

---

# FAST AND ACCURATE RECONSTRUCTION OF PAN-TILT RGB-D SCANS VIA AXIS BOUND REGISTRATION

---

A PREPRINT

**Jung-Hyun Byun**  
Department of Computer Science  
Yonsei University, Korea  
junghyun.ian.byun@gmail.com

**Tack-Don Han**  
Department of Computer Science  
Yonsei University, Korea  
hantack55@gmail.com

November 3, 2022

## 1 Introduction

Indoor scene reconstruction is of crucial importance in various research areas, in which 3D geometry data is required, such as robotics, architecture, and augmented reality. More specifically, in robotics, 3D map data is required for a robot to localize itself, plan a path, and navigate to a specific location as ordered. The practice of this localization and mapping is often abbreviated as SLAM (Simultaneous Localization and Mapping) [1, 2]. In architecture, indoor scenes are reconstructed, so that users can navigate virtually, and are then exported as CAD files for users to correct reconstruction errors and further edit to meet their needs [3]. In conjunction with augmented reality (AR), reconstructed models are used as graphics scene files, on which users can superimpose virtual objects before actually installing them [4], or are used as surface geometry for projection-based AR, where geometric distortions are corrected to deliver pure immersive AR experience [5, 6].

In general, RGB depth (RGB-D) cameras are hand-held by the user and are moved freely around the environment to map and reconstruct the geometry of indoor scenes, particularly for SLAM applications [7]. However, in various cases, RGB-D cameras are attached to pan-tilt rotating platforms and collect 3D data captured in pan-tilt sweeps [4, 8, 9, 5, 6]. Using pan-tilt platforms with RGB-D cameras has several advantages. Namely, the field-of-view of the cameras is limited when a wide range of data is captured from the environment, and rotating the camera by pan-tilt units is preferred [10] over noisy hand-held alternatives. Moreover, using pan-tilt RGB-D cameras in the center of a standard-sized room, is an ideal option for capturing room geometry [8] if the stationary nature of the scene and the ranging limit of the RGB-D camera (typically 1.5–4.5 m) are taken into account. Finally, as the scanning and capturing process can be automated and computer-controlled [4, 9], it would be more convenient and accurate to use pan-tilt RGB-D cameras.

As SLAM methods can perform localization of the camera that is freely moving and mapping of the environment at the same time, some pan-tilt setups adopts SLAM methods for such purposes. For example, Beamatron [5] is a steerable projection augmented reality system, where a projection and a Microsoft Kinect 360 were mounted on a pan-tilt moving light platform. Beamatron used the well-known KinectFusion [11] to reconstruct the surface geometry on which the projection was mapped. However, even though SLAM methods such as KinectFusion are able to reconstruct indoor scenes reliably, their typical reliance on the iterative closest point (ICP) algorithm [12] makes the overall process exhaustive and iterative. Thus, several ICP-based SLAM methods support real-time performance only with the assistance of massively parallel programming, namely general-purpose computing on graphics processing units (GPGPU) [13].

The prerequisite for GPU equipment of the SLAM approach sets a limitation for its applicability to low-powered computing devices that are without additional hardware. However, ICP-based SLAM methods would not be a necessity to track the camera pose or reconstruct the environment, if some prior knowledge of the camera motion is known, such as a pan-tilt platform. In this study, a fast and accurate registration algorithm, called *axis bound registration*, is proposed that can be used in such a configuration, where an RGB-D camera on a pan-tilt platform is rotated to acquire scan data for reconstructing indoor environments. Exploiting the fact that the movement of the camera is bound by

the two rotation axes of the servo motors, the proposed algorithm is able to produce comparable or better registration results in much shorter time, when compared to other state-of-the-art registration and SLAM methods.

The proposed *axis bound registration* is not technically a SLAM. However, the proposed method and SLAM methods have certain similarities: The proposed method models the motions of the camera (on a pan-tilt platform), estimates its pose changes (along the trajectory of rotations), and uses the acquired information to reconstruct the scene (by point cloud registration). Thus, the proposed method may be considered an alternative to SLAM methods when pan-tilt RGB-D camera systems are used, such as Beamatron [5] or AIR [6]. The results in Table 2 support the claim that the proposed method offers a lighter and more accurate option for scene reconstruction in pan-tilt cases. This is possible due to several novelties and contributions of the proposed *axis bound registration*, which are as follows:

1. The proposed method models the rotational motion of the pan-tilt platform, and thus it can estimate unseen poses of pan-tilt rotations. This is possible by prior knowledge acquired through modeling and recovering parameters of the rotation axes.
2. A novel rotation trajectory-based keypoint matching and rejection method is developed to further refine the estimated pose during online operation. This mitigates any negative effects of possible errors from the calibration process on pose estimation.
3. The alternating optimization removes most of the iterative nature of non-linear optimization in the pairwise registration process. This results in greatly improved registration accuracy/speed and convergence in the iterative closest point (ICP) process.

Overall, the proposed method outperforms state-of-the-art algorithms of various approaches based on camera calibration, global registration, and localization mapping in terms of root-mean-square-error (RMSE) and computation time.

In the following sections, a step-by-step approach to performing *axis bound registration* will be presented, which is the key algorithm of the proposed method. In Section 2, a review of related studies is presented. In Sections 3.1 and 3.2, the rotation axes of a pan-tilt platform are calibrated. In Section 3.4, the calibrated rotation parameters are then recovered in the *global* frame coordinates, so that all *local* point clouds may be registered in a common frame, using the global transformation model of Equation 8. In Section 4.1, the rotated angles of each *local* frame around the calibrated rotation axes are computed and the servo control mechanism that converts applied pulses to rotation angles is identified. Using the rotation parameters in the *global* frame and rotation angles, the current pose of the pan-tilt camera can be estimated and used to roughly register two point clouds globally in Section 4.2. In Section 4.3, the proposed method that further optimizes local registration results in a pairwise manner is explained using trajectory-constraint-based matching and rejection, and finally, the *axis bound registration* method is presented. In Section 5, the experiment design and configurations are described. Moreover, the performance of the proposed method against four other state-of-the-art registration methods is evaluated and validated.

## 2 Related Work

### 2.1 Rotation Axis Calibration

As explained above, the proposed axis bound registration method extends pan-tilt axis calibration to achieve point cloud registration. It was inspired from various previous studies. The first to be reviewed are those from the computer vision field, where pan-tilt-zoom (PTZ) cameras have long been used for surveillance, object tracking and so forth. Davis and Chen in [14] presented a calibration model where the typical pin-hole camera model was extended to incorporate the characteristics of pan and tilt motions. Its most significant contribution is a pan-tilt assembly model that accurately reflects the motion and structure of a general pan-tilt camera, in which the pan and tilt axes are modeled independently from the axes of the camera frame. In [15], Wu and Radke proposed a camera model involving not only pan and tilt motions but also zoom on the image domain. They also reported their observations on the behavior of pan-tilt motors and categorized several errors that can arise during the operation of a PTZ camera.

In the optics and measurement literature, a calibration method for a rotating turntable was introduced in [16]. In the proposed setup, in contrast to a typical PTZ camera setup, the camera was fixed, whereas a checkerboard was attached to a turntable and rotated to acquire the rotation axis with respect to the fixed camera. Here, constrained global optimization and the least squares method were used to solve the great circle equations, which are used as models for the rotation trajectories. The method was later extended by Niu et al. in [10], where the camera itself was attached to a rotating plate. A regular RGB camera was used, and thus the camera could not directly see the rotation axis. Accordingly, another external camera was used as a global reference frame, and the rotation axis was computed with regard to the external camera.

Byun et al. in [17] proposed a control mechanism for manipulating the motion and orientation of a generalized pan-tilt camera. Combining rotation axis calibration and camera-servo control, the authors were able to control the camera and accurately target a designated mark, based on the inverse kinematics approach. Even though their method was accurate, it relied on iterative and time-consuming Jacobian optimization and did not incorporate random errors that can occur during operation, as reported in [15]. The proposed method significantly extends the method in [17] by incorporating a random servo error handling mechanism and registering RGB-D scans based on the pan-tilt camera motion and control model.

## 2.2 Point Cloud Matching

[18] defines the point registration as the process of acquiring a transformation between two point clouds that determines the mapping relationship in the 3D space. [19] and [18] categorized point cloud registrations into three types, namely, global, local, and local descriptor registration. Global registration is a method that globally searches the point correspondences given two point clouds of any condition. By contrast, local registration methods require the input point clouds to be as close and overlapping as possible for the methods to work properly. Local descriptors registration involves a matching process of feature descriptors to determine point correspondences.

Super 4-points congruent sets (Super4PCS) [19] and fast global registration (FGR) [20] are examples of global registration methods. The authors of [19] proposed a novel method for removing the quadratic time complexity of its predecessor in [21]. The key idea behind this improvement is the use of the data structure in solving the core instance problem, where the goal is to find all candidate pairs of a given point that are within a distance range. FGR optimizes an objective function involving candidate matches over the surface of the object scans to align surfaces. The authors argue that the method does not require initialization, yet it can achieve accuracy comparable to that of well-initialized local refinement algorithms. Both global registration methods are compared with the proposed method in Section 5.

The proposed method adopts the coarse-to-fine registration scheme, where in the coarse registration step the two given RGB-D frames are brought to the same *global* coordinates, and in the fine registration step, the source frame is *locally* transformed and aligned to match the target frame. The *global* transform is achieved by modeling and recovering the rotation motions of the pan-tilt system. In the *local* transform, the keypoints are extracted and matched. False-matched keypoints are rejected by their distances to the rotation trajectory of the target points, and the remaining pairs are used to compute the transformation that brings corresponding points together, while keeping the transformations bound to the rotation trajectory. In this sense, the proposed method can be regarded as a hybrid global and local registration method, where the coarse registration step can be thought of as the global registration, and the fine registration step as the local registration.

## 2.3 Localization and Mapping

Research in the SLAM field focuses on positional, orientational tracking of the camera and reconstruction of the scene in tandem. Past studies on SLAM include MonoSLAM [22], which is based on the input of a single commodity sensor that is a monocular RGB camera, parallel tracking and mapping [23], which is more accurate, and DTAM [24], which combines camera tracking with dense surface reconstruction.

As mentioned above, some SLAM methods rely on the ICP algorithm [12] to track the pose of the camera. For example, [1] tracks the pose of the camera by repeatedly revising the transformation (translation and rotation) required for minimizing the difference between two clouds of points based on ICP. KinectFusion [11] and RGB-D SLAM [25] also depends on ICP to densely track the 3D pose of the Kinect sensor and reconstruct 3D surface models of the environment. In [26], ICP was used to add a graphical model layer that registers point clouds to optimize the pose graph and the odometry.

Even though the ICP algorithm is straightforward and functional, its exhaustive and iterative nature makes SLAM methods inherently heavyweight in terms of computing resources, such as power and memory consumption. Thus, several ICP-based SLAM methods is able to perform in real-time only with the assistance of GPGPU [13]. This includes [11], [25] or ElasticFusion [27], which all makes significant use of the GPGPU computation for mapping construction as well as pose reconstruction and tracking.

Recently, a novel ORB-SLAM2 method was proposed in [2] that accepts any camera type (stereo, RGB-D, or monocular) and creates synthetic stereo coordinates of extracted features. The authors explain that their method, based on bundle adjustment, achieves a globally consistent sparse reconstruction and is thus sufficiently lightweight to work with standard central processing units (CPU). However, even ORB-SLAM2 relies on CPU multi-threading, OpenMP in this case, to achieve real-time performance, and it is observed that the execution time degrades to one frame per second without multi-thread support (see results in Table 3).

### 3 Pan–Tilt Rotation Model

To accurately and efficiently register pan–tilt scans of an RGB-D camera, the proposed approach takes into account the fact that the camera movement on a pan–tilt platform can be estimated by modeling and calibrating the rotation parameters of the pan–tilt platform. To generalize the proposed method as much as possible, it is assumed that no detailed information regarding the pan–tilt system, such as its assembly configuration or factory calibration, is given. To model the rotational motion of such generalized systems, the pan–tilt assembly model in [14] is adopted. The axes of pan and tilt rotations are not assumed to intersect the optical center of the camera, or to be precisely axis-aligned/orthogonal to each other. Pan and tilt motions modeled as rotations around arbitrary axes in space are shown in Figure 1. It should be noted that all transformations described hereafter are in a right-handed coordinate system, where the right, up, and front of the camera point in the  $X+$ ,  $Y+$ , and  $Z-$  directions, respectively.

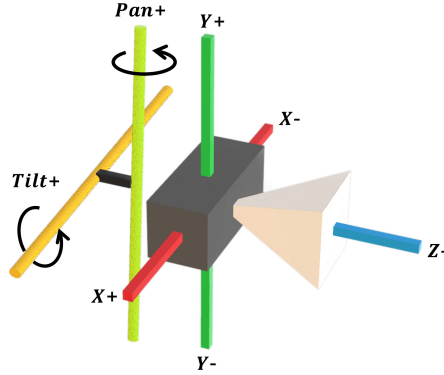


Figure 1: Pan–tilt rotation axis model and the camera system [17].

#### 3.1 Pan–tilt Calibration Process

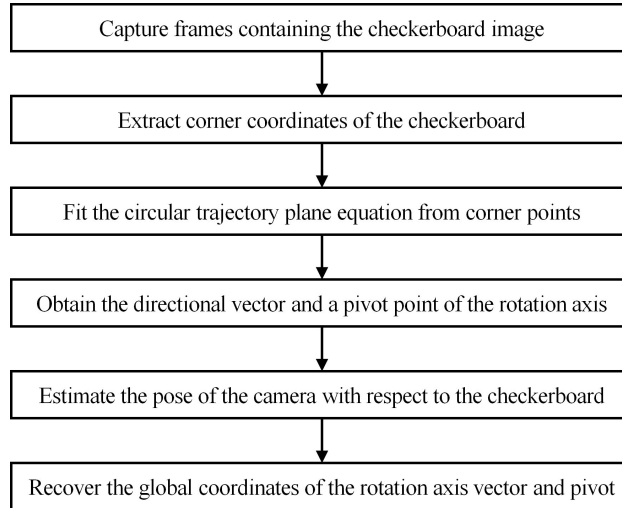


Figure 2: Procedure for calibrating the rotation axis.

To calibrate the axes of *pan* and *tilt* rotations, the method of Chen et al. [16] is employed, which was originally designed to calibrate the rotation axis of a turntable with a fixed camera. This is opposite to the aim of rotating the camera itself. However, as all transformations can be thought of as relative motions, one need only reverse the direction of the rotation, *i.e.*, the sign of the angle, after all rotation parameters are recovered. As the exact rotation axes are not known to recover the pose in the *global* frame before the calibration, the *pan* and *tilt* axes are first calibrated in some *reference* frame. Then, the relative pose of the *reference* frame to the *global* frame is computed and the parameters are recovered in *global* coordinates later. The overall process for calibrating the rotation axis is shown in Figure 2.

First, an arbitrary *reference* frame is set as a base. Then, the system rotates itself by a certain step using some units (in the present case, pulse width modulation or PWM is used). While rotating, the camera captures the coordinates of the checkerboard corners and saves them after converting them into depth camera coordinates, with the pulse width applied to the servo motor. These steps are iterated after the rotation is reversed until the checkerboard is out of the camera's view, at which point the system now calibrates the axis vector and center point of the rotation. The same process is performed twice, once for *pan* and once for *tilt*. The initial pose of the *reference* frame, represented by two rotation angles  $\theta_{tilt}$  and  $\theta_{pan}$ , can be estimated based on the normal vector of the checkerboard. The *local pan* and *tilt* rotation axes are converted into *global* coordinates, and the mapping relation of the rotation angle is determined to estimate the position and orientation of the camera.

### 3.2 Rotation Axis Calibration

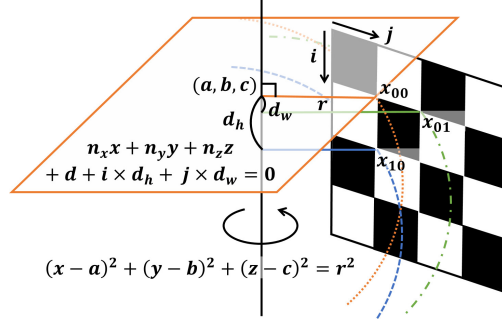


Figure 3: Schematic diagram for the rotation axis calibration model [17].

The proposed *axis bound registration* method requires calibration and modeling of the rotational motions of the *pan* and *tilt* servo motors. The steps in [17] are followed to recover their parameters for the rotation model, which is shown in Figure 3. The calibration process is divided into two sub-processes, where the direction vector of the rotation is first estimated by plane fitting, and the rotation trajectory is estimated by circle fitting. During the calibration, a large checkerboard is placed in front of the camera, vertical to the ground plane. Then, the camera is rotated clockwise and counter-clockwise until the checkerboard is out of view in the captured image, at both ends of the field-of-view, collecting as many frames of the checkerboard as possible. Based on the checkerboard normal, the *reference* pose in the *global* frame is later estimated.

Rotating arbitrary points around a rotation axis forms closed, circular trajectories, which can be represented as great circles on 3-dimensional planes, with the plane normals being rotation axes and the circle centers representing pivot points. Let  $l$  denote the count of the frames captured throughout the calibration process. Then, there exist in total  $l$  instances of a certain point, one from each captured frame. These  $l$  coordinates from multi-view frames can be used to obtain the circular trajectory of this certain point using the global least squares method [28], as in [16, 17]. Here, arbitrary points are corners on the checkerboard plane, with their geometrical relationship pre-known. Thus, all rotation trajectories are not independent, and can be represented relative to that of the top-leftmost corner. Then, the model can be parameterized from all corners of all frames, and the objective function can be globally optimized. Assuming that the checkerboard comprises  $m$  rows and  $n$  columns of corners,  $l \times m \times n$  corners in total can be used in the global optimization.

Let the rotation direction vector be defined as  $n = [n_x, n_y, n_z]^T$ , with its norm being  $\|n\| = 1$ , and the rotation center for the upper-left corner be defined as  $p = [a, b, c]^T$ . Then the line equation defining its rotation axis in 3D space is

$$\frac{x-a}{n_x} = \frac{y-b}{n_y} = \frac{z-c}{n_z}. \quad (1)$$

Furthermore, let the plane on which the circular trajectory of the rotation lies and that is  $d$  millimeter away from the origin be defined as

$$n_x x + n_y y + n_z z + d = 0. \quad (2)$$

The rotation circles of checkerboard corners have the same rotation axis, and the corners have the same geometric structure as the checkerboard. Therefore, their rotation centers, which are defined on the same line by Equation 1, can be represented using the interval terms in conjunction with the row and column indices. Let the distances of the intervals between each corner-plane be denoted by  $d_h$  and  $d_w$  (vertically and horizontally), respectively. Then, the

rotation circle center of an arbitrary corner on the  $i$ -th row and  $j$ -th column of the checkerboard can be denoted by  $p_{ij} = [a_{ij}, b_{ij}, c_{ij}]^\top$ , where

$$\begin{aligned} a_{ij} &= a - n_x(id_h + jd_w), \\ b_{ij} &= b - n_y(id_h + jd_w), \\ c_{ij} &= c - n_z(id_h + jd_w). \end{aligned} \quad (3)$$

The rotation trajectory is ideally modeled as a great circle in 3D space, which is uniquely and jointly defined by a plane and a sphere intersecting the plane. Here, the plane is modeled with parameters as

$$n_x x + n_y y + n_z z + d + id_h + jd_w = 0, \quad (4)$$

and the sphere as

$$(x - a_{ij})^2 + (y - b_{ij})^2 + (z - c_{ij})^2 = r_{ij}^2, \quad (5)$$

where  $l$  is the count of captured frames,  $m$  is the count of checkerboard rows, and  $n$  is the count of columns corners, as defined above. Let  $[x_{ijk}, y_{ijk}, z_{ijk}]^\top$  denote the 3D coordinates of the checkerboard corner on the  $i$ -th row and  $j$ -th column in the  $k$ -th captured frame. Then, a cost function is constructed to compute the parameters  $n_x, n_y, n_z, d, d_h, d_w$  minimizing the error of violating the plane model constraint, as follows:

$$\sum_{k=0}^{l-1} \sum_{i=0}^{m-1} \sum_{j=0}^{n-1} (n_x \cdot x_{ijk} + n_y \cdot y_{ijk} + n_z \cdot z_{ijk} + d + i \cdot d_h + j \cdot d_w)^2. \quad (6)$$

With parameters recovered from Equation 3 and their relationship in Equation 6, another cost function is constructed to identify the values of the parameters  $a, b, c, r_{ij}$  minimizing the error of violating the circle model constraint, as follows:

$$\sum_{k=0}^{l-1} \sum_{i=0}^{m-1} \sum_{j=0}^{n-1} ((x_{ijk} - a_{ij})^2 + (y_{ijk} - b_{ij})^2 + (z_{ijk} - c_{ij})^2 - r_{ij}^2)^2. \quad (7)$$

All  $l \times m \times n$  coordinates of checkerboard corners in multi-view frames are used to minimize two cost functions. The optimization is carried out using the global least squares method, which determines the optimal values for the rotation parameters [16].

### 3.3 Pan-Tilt Transformation Model

In Section 3.2, the parameters for modeling the rotations, namely, their axes and pivot points, were calibrated. With all the parameters of *pan* and *tilt* rotations calibrated, the corresponding coordinates of 3D points between a *local* camera frame and the *reference* frame can now be represented. If the *pan* and *tilt* angles of the *local* frame are denoted by  $\alpha$  and  $\beta$  respectively, and the local point by  $P_{local}$ , its corresponding point in the *reference* frame can be modeled as follows [17]:

$$\begin{aligned} \begin{bmatrix} P_{ref} \\ 1 \end{bmatrix} &= T_{pan} R_{pan}(\alpha) T_{pan}^{-1} T_{tilt} R_{tilt}(\beta) T_{tilt}^{-1} \begin{bmatrix} P_{local} \\ 1 \end{bmatrix}, \\ \text{where } R(\theta) &= \begin{bmatrix} \cos \theta + n_x^2(1 - \cos \theta) & n_x n_y(1 - \cos \theta) - n_z \sin \theta & n_x n_z(1 - \cos \theta) + n_y \sin \theta & 0 \\ n_y n_x(1 - \cos \theta) + n_z \sin \theta & \cos \theta + n_y^2(1 - \cos \theta) & n_y n_z(1 - \cos \theta) - n_x \sin \theta & 0 \\ n_z n_x(1 - \cos \theta) - n_y \sin \theta & n_z n_y(1 - \cos \theta) + n_x \sin \theta & \cos \theta + n_z^2(1 - \cos \theta) & 0 \\ 0 & 0 & 0 & 1 \end{bmatrix} \quad (8) \\ \text{and } T &= \begin{bmatrix} 1 & 0 & 0 & a \\ 0 & 1 & 0 & b \\ 0 & 0 & 1 & c \\ 0 & 0 & 0 & 1 \end{bmatrix}. \end{aligned}$$

Here,  $R_{tilt}$  is a  $4 \times 4$  matrix representing the *tilt* rotation around its axis vector  $n = [n_x, n_y, n_z]^\top$  and  $T_{tilt}$  is a  $4 \times 4$  matrix that represents the position of the rotation axis  $c = (c_x, c_y, c_z)$  that uniquely defines the *tilt* rotation. Any point on the line of the rotation axis can be a pivot for the rotation, which does not affect the final transformation. Here, the center point of the rotation of the upper-leftmost corner of the checkerboard was used. The same representation applies to the *pan* transformation.

It should be noted that the modeling was performed so that the system first tilts and then pans. This is to reflect the kinematic properties of the actual pan-tilt system that was used. As shown in Figure 8, the tilting arm is attached to the platform that is rotated by the panning servo motor. Thus, by applying the *tilt* transformation first and then the *pan* transformation, their rotations can be uniquely represented in the *global* system.

### 3.4 Rotation Parameterization in Global Frame

The parameters obtained in Section 3.2, however, are in the arbitrary *reference* coordinate system. This implies that all transformations using Equation 8 are in the *reference* frame. As the *reference* frame is arbitrarily chosen in Section 3.1, these parameters, two axes  $n_{pan}, n_{tilt}$  and two pivots  $c_{pan}, c_{tilt}$ , should be recovered in the *global* frame. The *global* frame is defined as the coordinate system of the RGB-D camera when it is directly facing the checkerboard and is perpendicular to the ground plane. The angles of *pan* and *tilt* rotations are defined as zero when the camera is in such a pose, and are denoted by  $\theta_{pan}$  and  $\theta_{tilt}$  when the camera is in the *reference* frame. The  $\theta_{tilt}$  and  $\theta_{pan}$  angles of the *reference* frame can be calculated based on the normal vector of the checkerboard.

To calculate the normal vector of the checkerboard plane, principal component analysis (PCA) is performed on the checkerboard corners. The corners are first translated so that their mean is equal to zero. Then, the covariance matrix of the checkerboard corners is considered. Decomposing the covariance matrix into eigenvectors and using the corresponding eigenvalues yields the estimate of the plane orthogonal basis. The normalized eigenvector corresponding to the minimum eigenvalue is the minimum mean square error solution to the plane normal estimation. The above covariance matrix  $Q$  can be expressed as follows:

$$\text{Where } \begin{bmatrix} \bar{x} \\ \bar{y} \\ \bar{z} \end{bmatrix} = \frac{1}{mn} \sum_{i=0}^{m-1} \sum_{j=0}^{n-1} \begin{bmatrix} x_{ij} \\ y_{ij} \\ z_{ij} \end{bmatrix}, \quad (9)$$

$$Q = \sum_{i=0}^{m-1} \sum_{j=0}^{n-1} \begin{bmatrix} (x_{ij} - \bar{x})^2 & (x_{ij} - \bar{x})(y_{ij} - \bar{y}) & (x_{ij} - \bar{x})(z_{ij} - \bar{z}) \\ (x_{ij} - \bar{x})(y_{ij} - \bar{y}) & (y_{ij} - \bar{y})^2 & (y_{ij} - \bar{y})(z_{ij} - \bar{z}) \\ (x_{ij} - \bar{x})(z_{ij} - \bar{z}) & (y_{ij} - \bar{y})(z_{ij} - \bar{z}) & (z_{ij} - \bar{z})^2 \end{bmatrix}.$$

Comparing the checkerboard normal  $n_{board}$  with its projection onto the  $XZ$ -plane  $n_{proj}$  yields the  $\theta_{tilt}$  angle, whereas comparing the projection with the optical axis, or the  $Z$ -axis, yields the  $\theta_{pan}$  angle by the following equation:

$$\begin{aligned} \text{Where } n_{proj} &= n_{board} \cdot [1, 0, 1]^T, \\ \theta_{tilt} &= \arccos(n_{proj} \cdot n_{board} / |n_{proj}| |n_{board}|) \\ \text{and } \theta_{pan} &= \arccos(n_{proj} \cdot [0, 0, 1]^T / |n_{proj}| |1|). \end{aligned} \quad (10)$$

These angles are substituted into Equation 8. Parts of the equation are rewritten to shorten it:  $F_{tilt}(\theta_{tilt}) = T_{tilt} R_{tilt}(\theta_{tilt}) T_{tilt}^{-1}$  and  $F_{pan}(\theta_{pan}) = T_{pan} R_{pan}(\theta_{pan}) T_{pan}^{-1}$ . Then the relation equation becomes

$$\begin{bmatrix} P_{global} \\ 1 \end{bmatrix} = F_{pan}(\theta_{pan}) F_{tilt}(\theta_{tilt}) \begin{bmatrix} P_{ref} \\ 1 \end{bmatrix}. \quad (11)$$

As noted in Section 3.3, tilting precedes panning. This implies that the *tilt* parameters calibrated in Section 3.2 are not affected by the initial  $\theta_{pan}$  rotation, or  $F_{pan}(\theta_{pan})$ . That is, the calibrated  $n_{tilt}$  and  $c_{tilt}$  are actually in the *global* frame, and thus no additional transformation is required. By contrast, the *pan* parameters are computed after the initial  $\theta_{tilt}$  transformation has been applied. Therefore, in the case of *pan*,  $F_{tilt}(\theta_{tilt})$  should be applied to the pivot translation to recover its position in the *global* frame. The *pan* axis, unlike its pivot, is a vector, not a point. Thus, only the rotation, without translation, should be applied. The above transformation can be summarized as follows:

$$\begin{aligned} \begin{bmatrix} n_{pan|global} \\ 1 \end{bmatrix} &= R_{tilt}(\theta_{tilt}) \begin{bmatrix} n_{pan|ref} \\ 1 \end{bmatrix} \quad \text{and} \\ \begin{bmatrix} c_{pan|global} \\ 1 \end{bmatrix} &= T_{tilt} R_{tilt}(\theta_{tilt}) T_{tilt}^{-1} \begin{bmatrix} c_{pan|ref} \\ 1 \end{bmatrix}. \end{aligned} \quad (12)$$

The final transformation equation of a point to *global* coordinates is not different from Equation 8, except that as the transformation is now from the *reference* frame to the *global* frame instead of the *local* and *reference*, the *global* parameters recovered above should be used and the subscripts should change accordingly.

## 4 Pan–Tilt Axis Bound Registration

In this section, we explain the pan-tilt axis bound registration, which is the key approach of the proposed method. It should be noted that the proposed method is inspired by [18] and [17]. However, it distinctively differs from and extends the original approaches. A brief overview, including motivation, contributions, and limitations, of these two studies is first presented.

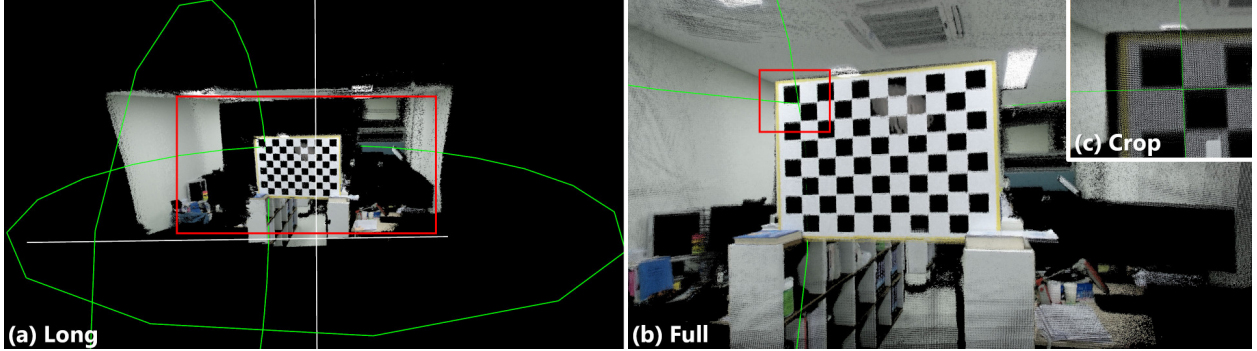


Figure 4: Pan/tilt calibration visualization in (a) long shot, (b) full frame, (c) cropped corner. Green circles denote rotation trajectories. White lines denote rotation axes. Red rectangles denote magnified regions. The rotation trajectories are calibrated with respect to the top-leftmost corner, and thus exactly coincide at the corner point.

In [18], an indoor scene point cloud registration method is proposed, where a pan-tilt RGB-D camera is used to capture and register point clouds. Multi-view calibrations are conducted to obtain the extrinsic parameter matrices with regard to the initial world coordinates prior to the point cloud registration process. The transformation matrices are stored and used as rough estimations for point cloud registrations during online operation. As the camera calibration from multiple viewpoints is performed offline using a known-geometry object, such as a checkerboard, the computation time for the transformation estimation is greatly reduced and the alignment precision is increased. However, as stated in [18], the method suffers from errors propagated from the calibration process, which leads to inaccurate point cloud alignments. Furthermore, the method cannot estimate the pose of the camera if the pan-tilt platform rotates to any unseen angles, as the transformation matrices should be calculated beforehand.

To tackle the issues in [18], the proposed *axis bound registration* method is based on the pan-tilt camera control method of [17]. The authors proposed a mechanism for accurate control of a pan-tilt system with an RGB-D camera. They formulated pan-tilt rotations as motions along great circle trajectories and calibrated their model parameters in 3D space, such as positions and vectors of rotation axes. The original study [17] focused on accurately controlling the pose of the camera, namely, orienting to and targeting at a designated mark, by optimizing the rotation angles of its transformation using inverse kinematics based on the Jacobian transpose method. The present study branches out from the camera control method into online pan-tilt pose estimation and the axis bound registration, using a different alternating optimization method.

#### 4.1 Camera Transformation with Servo Control

The proposed method aims at fast and accurate registration of point clouds of pan-tilt scans. The key motivation for this approach is that a rough estimate of the camera’s pose in the *global* system can be obtained based on the servo control. The rotation parameters in the *global* frame and the initial pose of the *reference* are recovered in Section 3.4. The effect of servo control on the rotation angle of the pan-tilt platform should now be considered.

Servo motors use potentiometers to orient themselves to certain directions. When a pulse of a certain width is applied, the servo rotates a by certain portion of its rotation range linearly with respect to its duty cycle. Therefore, it is possible to estimate the rotated angle of the pan-tilt platform based on the width of the applied pulse by the following relationship:

$$pulse\ width = scale \times angular\ degree + offset \quad (13)$$

As the above equation is a linear regression model, the solutions for *scale* and *offset* can be conveniently obtained by minimizing least square errors when an adequate amount of paired  $\{pulse\ width, angular\ degree\}$  data is given. During the rotation axis calibration process, the pulse widths applied to *pan* and *tilt* servos to orient the RGB-D camera are also saved to be input to Equation 13. Based on Equation 8, one can calculate the angles of each *l* *local* frame rotated from the *reference* frame using  $m \times n$  corner points of the checkerboard.

In Section 3.4, the initial pose of the *reference* frame,  $\theta_{pan}$  and  $\theta_{tilt}$ , was acquired. Substituting the values of  $\theta_{pan}$  or  $\theta_{tilt}$  into Equation 8 yields transformations that are solely based on *pan* or *tilt* rotations. Because *pan* and *tilt* rotations are separately calibrated, as mentioned in Section 3.1, these transformations can be used to compute the angular degrees by which each captured *local* camera frames rotated during the rotation axis calibration process. For simplicity, only

the case of *pan* rotation is considered. Substituting  $\theta_{tilt}$  into Equation 8 yields the following equation:

$$\begin{aligned} \begin{bmatrix} P_{global} \\ 1 \end{bmatrix} &= T_{pan} R_{pan}(\alpha) T_{pan}^{-1} \begin{bmatrix} P'_{local} \\ 1 \end{bmatrix}, \\ \text{where } \begin{bmatrix} P'_{local} \\ 1 \end{bmatrix} &= T_{tilt} R_{tilt}(\theta_{tilt}) T_{tilt}^{-1} \begin{bmatrix} P_{local} \\ 1 \end{bmatrix}. \end{aligned} \quad (14)$$

Here,  $P_{global} = [g_x, g_y, g_z]^T$  are the coordinates of  $m \times n$  checkerboard corners of the *reference* frame represented in the *global* system.  $P_{local} = [l_x, l_y, l_z]^T$  are the coordinates of checkerboard corners of each  $l$  *local* frame, with  $P'_{local} = [l'_x, l'_y, l'_z]^T$  being its *tilted* form. Only  $\alpha$ , which represents the rotation angle around the *pan* axis, is an unknown variable in the form of *sin* and *cos* in the equation. Simplifying Equation 14 with respect to  $\sin(\alpha)$  and  $\cos(\alpha)$  yields

$$\begin{aligned} A(\theta_{tilt}) \begin{bmatrix} \cos(\alpha) \\ \sin(\alpha) \\ 1 \end{bmatrix} &= \begin{bmatrix} g_x \\ g_y \\ g_z \end{bmatrix}, \text{ where } A(\theta_{tilt}) = \begin{bmatrix} \textcircled{1} & \textcircled{2} & \textcircled{3} \\ \textcircled{4} & \textcircled{5} & \textcircled{6} \\ \textcircled{7} & \textcircled{8} & \textcircled{9} \end{bmatrix}, \\ \textcircled{1} &= c_x (n_x^2 - 1) - l'_x (n_x^2 - 1) + c_y n_x n_y + c_z n_x n_z - n_x n_y l'_y - n_x n_z l'_z \\ \textcircled{2} &= c_y n_z - c_z n_y - n_z l'_y + n_y l'_z \\ \textcircled{3} &= c_x - c_x n_x^2 + n_x^2 l'_x - c_y n_x n_y - c_z n_x n_z + n_x n_y l'_y + n_x n_z l'_z \\ \textcircled{4} &= c_y (n_y^2 - 1) - l'_y (n_y^2 - 1) + c_x n_x n_y + c_z n_y n_z - n_x n_y l'_x - n_y n_z l'_z \\ \textcircled{5} &= c_z n_x - c_x n_z + n_z l'_x - n_x l'_z \\ \textcircled{6} &= c_y - c_y n_y^2 + n_y^2 l'_y - c_x n_x n_y - c_z n_y n_z + n_x n_y l'_x + n_y n_z l'_z \\ \textcircled{7} &= c_z (n_z^2 - 1) - l'_z (n_z^2 - 1) + c_x n_x n_z + c_y n_y n_z - n_x n_z l'_x - n_y n_z l'_y \\ \textcircled{8} &= c_x n_y - c_y n_x - n_y l'_x + n_x l'_y \\ \textcircled{9} &= c_z - c_z n_z^2 + n_z^2 l'_z - c_x n_x n_z - c_y n_y n_z + n_x n_z l'_x + n_y n_z l'_y. \end{aligned} \quad (15)$$

It should be noted that the axis  $n = [n_x, n_y, n_z]^T$  and the center  $c = [c_x, c_y, c_z]^T$  of the *pan* rotation are written without *pan* subscripts for simplicity. Concatenating the matrices on left and right hand sides of Equation 15 vertically for all coordinates of  $m \times n$  corners results in an overdetermined linear system, whose solution can be obtained by the least squares method using singular value decomposition (SVD). The resulting  $\cos(\alpha)$ ,  $\sin(\alpha)$  can be converted to an actual angle, by  $\alpha = \arctan 2(\sin(\alpha), \cos(\alpha))$ .

By Equation 15, all rotation angles,  $angle_0, angle_1, \dots, angle_{l-1}$ , of  $l$  *local* frames captured during the calibration can be calculated. Using the collected pulse widths,  $pulse_0, pulse_1, \dots, pulse_{l-1}$ , a linear system can be constructed based on Equation 13:

$$\begin{bmatrix} pulse_0 \\ pulse_1 \\ \dots \\ pulse_{l-1} \end{bmatrix} = scale \times \begin{bmatrix} angle_0 \\ angle_1 \\ \dots \\ angle_{l-1} \end{bmatrix} + offset. \quad (16)$$

As before, the equation can be solved for *scale* and *offset* by the least squares method using SVD. The pitfall is that the differences between the values of *angle* and *pulse* are very large, by two to three orders of magnitude because rotations operate in the range of  $-180-180^\circ$ , whereas the pulse width varies from 600 to 2400 microseconds. This scale of difference can affect the quality of the solution. This may be resolved by setting the pulse width of the *reference* frame as the *offset* and solve for *scale* only with the differences, not the original values, of the pulse widths relative to each *local* frame. This brings down the order of magnitude difference to 0–1 and yields a more stable solution. After obtaining the solution, the *offset* is adjusted by the value of the initial pose angle,  $\theta_{pan}$  or  $\theta_{tilt}$ , multiplied by *scale*.

## 4.2 Global Registration

The motivation in this study is similar to that in [18] in the sense that advantage is taken of the pan–tilt system to estimate the current pose of the camera. The key difference is that the proposed method models the movement of the pan–tilt system, whereas [18] relies on a pre-constructed database. In [18], multi-view calibration was performed to compute the transformation matrices of each preset pan–tilt rotation. Then a database was constructed that stores all the matrices. Even though this approach saves computation time in the registration task, the method is limited in terms of scalability, as it is virtually impossible to record transformations of every possible pan–tilt point in the real world.

To tackle this issue, the rotation of a pan-tilt system is modeled and estimated, instead of creating and looking up a database.

The pan-tilt system is rotated by two servo motors, which are controlled according to the width of the applied pulse. Thus, by formulating the rotation angles of the servo motors and their transformation model, the overall transformation of the pan-tilt system can be identified. The rotation degree can be estimated by inputting the pulse width to Equation 13. The rotation angle is then substituted into Equation 8, yielding the final transformation matrix. The transformation matrix is an estimation of the camera pose in the *global* frame, which can be interpreted as the  $view^{-1}$  matrix in *graphics* terms. Here, point clouds are captured in *local* camera coordinates, implying that their *model* matrices are actually the  $view^{-1}$  matrix of the camera. Thus, the camera pose in the *global* frame, which is used to convert *local* coordinates of 3D points in the camera frame to *global* coordinates [17], can be also used as a rough estimation for registering point clouds.

### 4.3 Local Registration

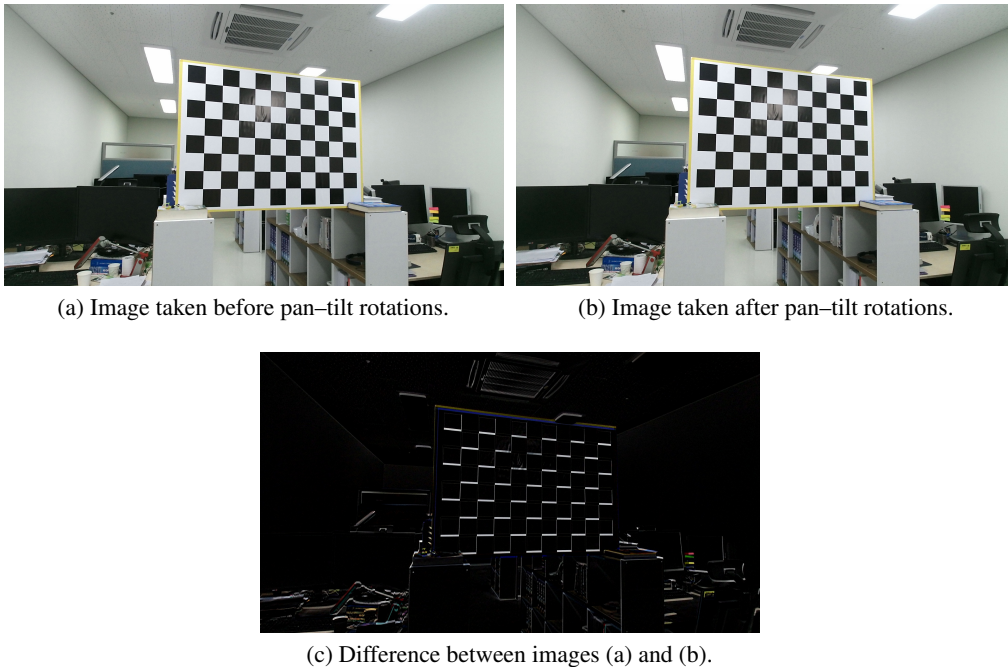


Figure 5: Random errors of the pan-tilt system. Two frames (a) and (b) are captured at the same servo position, in terms of PWM. Thus, they should be identical, but in reality they are not.

Even though the estimated pose of the pan-tilt camera can be used as a transform matrix for registering point clouds, it has its own limitations. One problem is the random error of a pan-tilt system, as illustrated in Figure 4 of [15]. The authors observed that the images taken at the very same position differ by 5–7 pixels of error when the pan-tilt system operates after 30 minutes of random motion. Such errors were also experienced in this study during calibration and experimentation with the pan-tilt system. The present version of the random error is illustrated in Figure 5. The presence of random errors of the pan-tilt system indicates that the transform matrices obtained in Section 4.2 are indeed merely a rough guess. Thus, the rough estimation of *global* transform should be refined in *local* registration.

#### 4.3.1 Rotation Trajectory-based Matching and Rejection

Given pairs of frames, including color images, depth images, and point clouds, the local registration is performed in a pairwise manner between two consecutive scenes. The common first step in pairwise registration would be feature extraction of and matching between two frames. Thus, pairwise local registration starts with feature matching. In this study, ORB (Oriented FAST and Rotated BRIEF) [29] keypoints and descriptors are used. The ORB feature is selected to remove any bias in the experiments comparing the present results with those in [2], where ORB features were used for SLAM as well. The details of the experiments will be explained in Section 5.

Simple matching of descriptors suffers from false positives and outliers. To resolve this, external methods are often employed. For example in [30], the authors employed the random sample consensus (RANSAC) tactic to subsample keypoints of an image. Then, knowing the shape of the target image, which was a planar rectangular object, they used the inverse homography method to validate whether the randomly sampled points were in accordance with the target image in a geometrical sense.

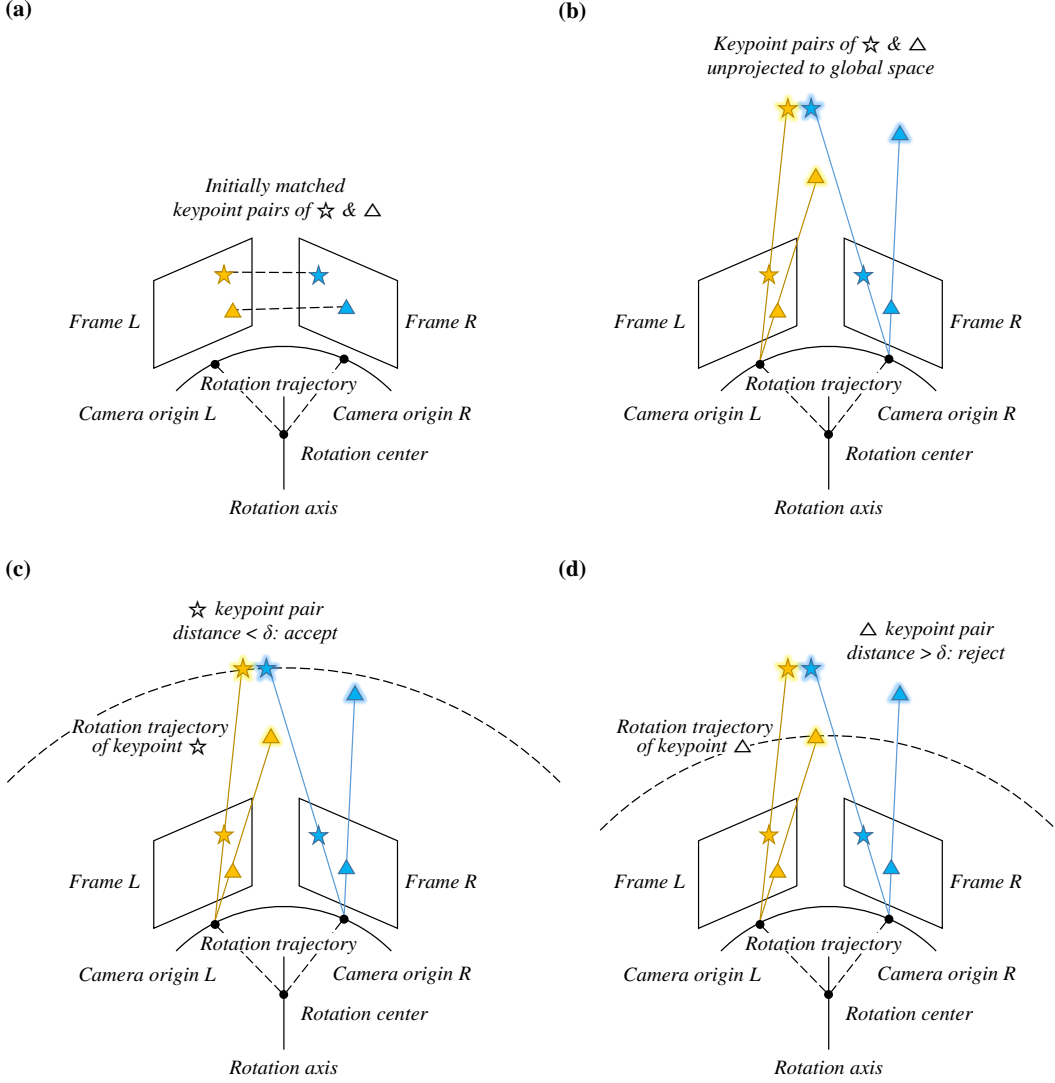


Figure 6: Schematic diagram for rejecting outlier matching pairs based on trajectory constraints.

- (a) Keypoint pairs between two proximate frames are matched in the 2D image domain.
- (b) Keypoints are unprojected to 3D points in *global* space, represented with halos.
- (c) Keypoints whose distance is below the threshold  $\delta$  are accepted as a correspondence pair.
- (d) Keypoints whose distance is above the threshold  $\delta$  are rejected as outlier matches.

Using the RANSAC method to remove outliers is a common approach. However, the iterative nature of random sampling inevitably results in extensive computational load for reaching consensus. Thus, a novel method is introduced whereby the geometric relationships obtained in Section 4.1 are used as trajectory constraints to reject false positives. The overall process and schematic diagram for determining and rejecting outliers are shown in Figure 6. Let the first and second frames of a given pair be denoted by  $l$  and  $r$ , respectively. A frame of pan-tilt scan data consists of a color (RGB) image, a depth image, and a point cloud. The objective is to align two point clouds  $P^l$  and  $P^r$ . First, ORB keypoints are extracted from two color images  $C^l$  and  $C^r$ , and are matched based on their descriptors. These keypoints in color image domains are then unprojected to 3D points in each *local* camera frame using depth data,  $D^l$  and  $D^r$ . The

two keypoints of a 3D keypoint pair are denoted by  $k_i^l$  and  $k_i^r$ , where the subscript  $i$  denotes the  $i$ -th keypoint pair. The pulse widths of each frame can be converted to *pan* and *tilt* angles in *global* space using Equation 13,  $\alpha^l, \beta^l, \alpha^r$ , and  $\beta^r$ .

Substituting  $k_i^l, \alpha^l, \beta^l$  into Equation 8 yields 3D points with *global* coordinates, which are denoted by  $\hat{k}_i^l$ . The corresponding keypoint  $\hat{k}_i^r$  of the  $r$  frame is obtained as follows:

$$\begin{aligned} \begin{bmatrix} \hat{k}_i^l \\ 1 \end{bmatrix} &= T_{pan} R_{pan}(\alpha^l) T_{pan}^{-1} T_{tilt} R_{tilt}(\beta^l) T_{tilt}^{-1} \begin{bmatrix} k_i^l \\ 1 \end{bmatrix}, \\ \begin{bmatrix} \hat{k}_i^r \\ 1 \end{bmatrix} &= T_{pan} R_{pan}(\alpha^r) T_{pan}^{-1} T_{tilt} R_{tilt}(\beta^r) T_{tilt}^{-1} \begin{bmatrix} k_i^r \\ 1 \end{bmatrix}. \end{aligned} \quad (17)$$

Given  $\hat{k}_i^l$  and  $\hat{k}_i^r$ , which are coordinates computed by initial estimations of the rotation angles, i.e.,  $\alpha^l, \beta^l, \alpha^r$  and  $\beta^r$ , it is determined whether they are falsely matched or not based on their distances. Specifically, the indicator function  $g(\hat{k}_i^l, \hat{k}_i^r)$  declares that the matching of  $\hat{k}_i^l$  and  $\hat{k}_i^r$  is a false positive if the distance exceeds a certain limit, namely  $\delta$ , as follows:

$$g(\hat{k}_i^l, \hat{k}_i^r) = \begin{cases} 0, & \text{if } \|\hat{k}_i^l - \hat{k}_i^r\|_2 > \delta \\ 1, & \text{otherwise} \end{cases} \quad (18)$$

Here,  $\|\cdot\|_2$  denotes the Euclidean distance function for the given input. As mentioned above, however, a pan-tilt system is inclined to introduce random errors in its rotation. Thus, even though the mapping between pulse width and rotation angle has been modeled by Equation 13, possible errors should be taken into account in the calculation of rotation angles. To mitigate the effect of the random errors on the indicator function  $g(\cdot, \cdot)$ , the threshold value of the distance  $\delta$  is defined with sufficient margins to prevent false-negative rejections. In the proposed setup used in Section 5,  $\delta$  was set to 100 *mm*. The feature matching and rejection result is illustrated in Figure 7.

### 4.3.2 Pairwise Axis Bound Transform Estimation

For clarity, the notations  $\hat{k}_i^l$  and  $\hat{k}_i^r$  are used to denote keypoint pairs that are determined as true-positives by Equation 18. It should be noted that in pairwise registration, the  $l$  frame is the target frame and  $r$  is the query. The target frame can be thought of as the *reference* frame and the query as the *local* frame in Equation 8. Then, the objective of local registration is to determine the pan-tilt angles of  $\alpha^r$  and  $\beta^r$  of the query frame that transforms  $k_i^r$  to its correspondence as  $\alpha^l, \beta^l$ , and  $\hat{k}_i^l$  of the target frame are fixed. It should also be noted that  $k_i^r$  is in the *local* frame, whereas  $\hat{k}_i^l$  is in the *global* frame. Formally, the cost function for the local registration task is constructed so as to minimize the distances between correspondence pairs after *global* transformation in Equation 19. The transformation regarding the cost function is bound by the two rotation axes, *pan* and *tilt*, hence the name *Axis Bound Registration* of the proposed algorithm. This is in contrast to several point-to-point registration approaches that commonly use simple yet more complex  $[R|t]$  six degrees-of-freedom (DoF) transformations [31]. Rotation axis calibration provides the prior knowledge of *pan* and *tilt* axes, which downsizes the overall problem to a two DoF problem about  $\alpha^r$  and  $\beta^r$ . This not only reduces computation complexity but also removes several ambiguities regarding the final transformation.

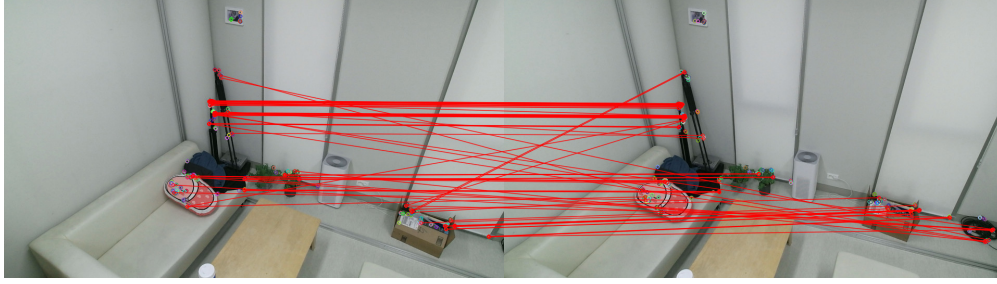
$$\arg \min_{\alpha^r, \beta^r} \sum_i^N \left\| \begin{bmatrix} \hat{k}_i^l \\ 1 \end{bmatrix} - T_{pan} R_{pan}(\alpha^r) T_{pan}^{-1} T_{tilt} R_{tilt}(\beta^r) T_{tilt}^{-1} \begin{bmatrix} k_i^r \\ 1 \end{bmatrix} \right\|_2^2, \quad (19)$$

where  $N$  is the number of matched keypoint pairs between frame  $l$  and  $r$ .

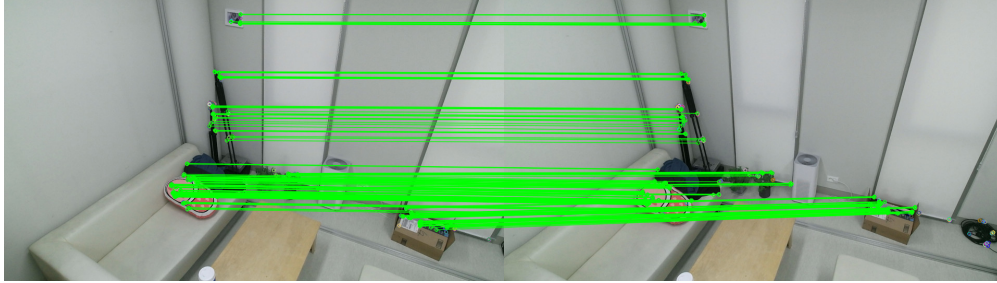
Obviously, the cost function in Equation 19 is a non-linear optimization problem about two variables  $\alpha^r$  and  $\beta^r$ , which are in the form of interdependent trigonometric functions  $\cos$  and  $\sin$ . It is a common practice to solve a non-linear optimization problem in an iterative manner, reducing numerical errors step-by-step. Taking [17] for example, the authors solved a similar problem, where the objective was to orient the camera so that it positions the target object at the center of the image. Adopting the inverse kinematics approach, they used the Jacobian transpose method [32] to iteratively minimize point-to-point distances. Likewise, relying on the inverse kinematics approach and iterative solving for two rotation angles in the proposed methods is a viable option. However, as iterative methods often hinder real-time performance, a more sophisticated scheme of alternating optimization is adopted, as was used in camera calibration implementation in the OpenCV library [33] (p.673), and camera pose optimization [34] (Section 4.3 Alternating Optimization). The alternating optimization scheme decomposes Equation 19 into two sub-problems, where  $\alpha^r$  is independently obtained with fixed  $\beta^r$  and vice versa. This continues iteratively until the system reaches numerical convergence. Even though the alternating optimization scheme itself does not solve the equation in a closed form, the sub-divided equations regarding  $\alpha^r$  and  $\beta^r$  can be solved in closed form, greatly reducing computational complexity. Moreover, it is empirically confirmed that the alternating optimization scheme solves Equation 19 in a semi-closed



(a) Initial matching result of 364 keypoint pairs (based on descriptor distance).



(b) Outlier rejection result of 97 keypoint pairs (based on trajectory distance).



(c) Final correspondence result of 267 keypoint pairs.

Figure 7: Illustration of (a) matching keypoints, (b) rejecting outliers, and (c) final corresponding pairs. Outliers are rejected if the distance in *global* coordinates to estimated pairs exceeds a certain threshold (e.g., 100 mm). Keypoint pairs with diagonal directions and weak correspondences are removed.

form, that is, a sufficiently optimal *local* registration solution is reached starting from a coarse *global* registration in a single step. The RMSE performance of the single-step alternating optimization scheme is discussed in Section 5.

A part of the alternating optimization scheme is already introduced in Equations 14 and 15. The fundamental ideas are the same. The difference is that the rotation angles for *tilt* are set according to Equation 13, not from the values obtained by the rotation axis calibration process. This is also the key difference from [18], where only rotation angles that are pre-acquired in the camera calibration process are stored and later used. Another difference is that matched keypoints are now used as *local-global* correspondence pairs, instead of checkerboard corners, thus compensating for random errors due to the servo motors [15] and further optimizing for better online local registration results.

Let  $\theta_{tilt}$  denote the given value for the *tilt* rotation. Then ideally, by the rotation transformation of Equation 8, the equation for the *pan* rotation angle  $\alpha$  can be modeled as follows:

$$\begin{aligned} \begin{bmatrix} \hat{k}_i^l \\ 1 \end{bmatrix} &= T_{pan} R_{pan}(\alpha) T_{pan}^{-1} \begin{bmatrix} k_i^{r'} \\ 1 \end{bmatrix}, \\ \text{where } \begin{bmatrix} k_i^{r'} \\ 1 \end{bmatrix} &= T_{tilt} R_{tilt}(\theta_{tilt}) T_{tilt}^{-1} \begin{bmatrix} k_i^r \\ 1 \end{bmatrix}. \end{aligned} \tag{20}$$

Similarly, let  $\theta_{pan}$  denote the given value for the *pan* rotation. Then ideally, by the rotation transformation of Equation 8, the equation for the *tilt* rotation angle  $\beta$  can be modeled as follows:

$$\begin{aligned} \begin{bmatrix} \hat{k}_i^l \\ \hat{k}_i^l \\ 1 \end{bmatrix} &= T_{tilt} R_{tilt}(\beta) T_{tilt}^{-1} \begin{bmatrix} k_i^r \\ k_i^r \\ 1 \end{bmatrix}, \\ \text{where } \begin{bmatrix} \hat{k}_i^l \\ \hat{k}_i^l \\ 1 \end{bmatrix} &= T_{pan}^{-1} R_{pan}(\theta_{pan}) T_{pan} \begin{bmatrix} \hat{k}_i^l \\ \hat{k}_i^l \\ 1 \end{bmatrix}. \end{aligned} \quad (21)$$

The  $r$  superscripts of  $\alpha$  and  $\beta$  are omitted for simplicity.  $\hat{k}_i^l$ ,  $\hat{k}_i^l$ ,  $k_i^r$ ,  $k_i^r$  are all 1-by-3 column vectors denoting  $XYZ$  coordinates in the 3D space. It should be noted that  $\hat{k}_i^l$  and  $k_i^r$  are introduced to incorporate known rotations of  $\theta_{tilt}$  and  $\theta_{pan}$ , respectively, for clarity. The cost function in Equation 20 can now be divided into two sub-cost functions as follows:

$$\arg \min_{\alpha} \sum_i^N \left\| \begin{bmatrix} \hat{k}_i^l \\ \hat{k}_i^l \\ 1 \end{bmatrix} - T_{pan} R_{pan}(\alpha) T_{pan}^{-1} \begin{bmatrix} k_i^r \\ k_i^r \\ 1 \end{bmatrix} \right\|_2^2 \quad (22)$$

and

$$\arg \min_{\beta} \sum_i^N \left\| \begin{bmatrix} \hat{k}_i^l \\ \hat{k}_i^l \\ 1 \end{bmatrix} - T_{tilt} R_{tilt}(\beta) T_{tilt}^{-1} \begin{bmatrix} k_i^r \\ k_i^r \\ 1 \end{bmatrix} \right\|_2^2. \quad (23)$$

Each sub-cost function can be alternately solved in closed form. The alternating optimization starts by substituting the initially estimated *tilt* rotation angle of Equation 13 into Equation 22 as  $\theta_{tilt}$ . Solving Equation 22 yields the value for  $\alpha$ , which is substituted into Equation 23 as  $\theta_{pan}$  and fixed. Solving Equation 23 yields the value of  $\beta$ .  $\beta$  can be in turn substituted into Equation 22 as  $\theta_{tilt}$ , which can be solved again for further optimization. Empirically, a single step suffices to yield numerically optimal solutions. To solve Equations 22 and 23, two linear systems similar to Equation 15 are constructed.

$$A(\theta_{pan}) \begin{bmatrix} \cos(\beta) \\ \sin(\beta) \\ 1 \end{bmatrix} = [\hat{k}_i^l], \text{ where } A(\theta_{pan}) = \begin{bmatrix} \textcircled{1} & \textcircled{2} & \textcircled{3} \\ \textcircled{4} & \textcircled{5} & \textcircled{6} \\ \textcircled{7} & \textcircled{8} & \textcircled{9} \end{bmatrix},$$

$$\begin{aligned} \textcircled{1} &= c_x (n_x^2 - 1) - x_i^r (n_x^2 - 1) + c_y n_x n_y + c_z n_x n_z - n_x n_y y_i^r - n_x n_z z_i^r \\ \textcircled{2} &= c_y n_z - c_z n_y - n_z y_i^r + n_y z_i^r \\ \textcircled{3} &= c_x - c_x n_x^2 + n_x^2 x_i^r - c_y n_x n_y - c_z n_x n_z + n_x n_y y_i^r + n_x n_z z_i^r \\ \textcircled{4} &= c_y (n_y^2 - 1) - y_i^r (n_y^2 - 1) + c_x n_x n_y + c_z n_y n_z - n_x n_y x_i^r - n_y n_z z_i^r \\ \textcircled{5} &= c_z n_x - c_x n_z + n_z x_i^r - n_x z_i^r \\ \textcircled{6} &= c_y - c_y n_y^2 + n_y^2 y_i^r - c_x n_x n_y - c_z n_y n_z + n_x n_y x_i^r + n_y n_z z_i^r \\ \textcircled{7} &= c_z (n_z^2 - 1) - z_i^r (n_z^2 - 1) + c_x n_x n_z + c_y n_y n_z - n_x n_z x_i^r - n_y n_z y_i^r \\ \textcircled{8} &= c_x n_y - c_y n_x - n_y x_i^r + n_x y_i^r \\ \textcircled{9} &= c_z - c_z n_z^2 + n_z^2 z_i^r - c_x n_x n_z - c_y n_y n_z + n_x n_z x_i^r + n_y n_z y_i^r. \end{aligned} \quad (24)$$

$$A(\theta_{tilt}) \begin{bmatrix} \cos(\alpha) \\ \sin(\alpha) \\ 1 \end{bmatrix} = [\hat{k}_i^l], \text{ where } A(\theta_{tilt}) = \begin{bmatrix} \textcircled{1} & \textcircled{2} & \textcircled{3} \\ \textcircled{4} & \textcircled{5} & \textcircled{6} \\ \textcircled{7} & \textcircled{8} & \textcircled{9} \end{bmatrix},$$

$$\begin{aligned} \textcircled{1} &= c_x (n_x^2 - 1) - x_i^{r'} (n_x^2 - 1) + c_y n_x n_y + c_z n_x n_z - n_x n_y y_i^{r'} - n_x n_z z_i^{r'} \\ \textcircled{2} &= c_y n_z - c_z n_y - n_z y_i^{r'} + n_y z_i^{r'} \\ \textcircled{3} &= c_x - c_x n_x^2 + n_x^2 x_i^{r'} - c_y n_x n_y - c_z n_x n_z + n_x n_y y_i^{r'} + n_x n_z z_i^{r'} \\ \textcircled{4} &= c_y (n_y^2 - 1) - y_i^{r'} (n_y^2 - 1) + c_x n_x n_y + c_z n_y n_z - n_x n_y x_i^{r'} - n_y n_z z_i^{r'} \\ \textcircled{5} &= c_z n_x - c_x n_z + n_z x_i^{r'} - n_x z_i^{r'} \\ \textcircled{6} &= c_y - c_y n_y^2 + n_y^2 y_i^{r'} - c_x n_x n_y - c_z n_y n_z + n_x n_y x_i^{r'} + n_y n_z z_i^{r'} \\ \textcircled{7} &= c_z (n_z^2 - 1) - z_i^{r'} (n_z^2 - 1) + c_x n_x n_z + c_y n_y n_z - n_x n_z x_i^{r'} - n_y n_z y_i^{r'} \\ \textcircled{8} &= c_x n_y - c_y n_x - n_y x_i^{r'} + n_x y_i^{r'} \\ \textcircled{9} &= c_z - c_z n_z^2 + n_z^2 z_i^{r'} - c_x n_x n_z - c_y n_y n_z + n_x n_z x_i^{r'} + n_y n_z y_i^{r'}. \end{aligned} \quad (25)$$

Here,  $k_i^r = [x_i^r, y_i^r, z_i^r]^\top$  and  $k_i^{r'} = [x_i^{r'}, y_i^{r'}, z_i^{r'}]^\top$ . In both Equations 24 and 25, concatenating both sides column-wise for  $N$  keypoint pairs results in two overdetermined linear systems. The systems are classic examples that can be solved by the SVD method, resulting in least squares error solutions for  $\cos(\beta)$ ,  $\sin(\beta)$ , and  $\cos(\alpha)$ ,  $\sin(\alpha)$ . The initial solutions are refined to obtain the actual rotation angles of interest by enforcing trigonometric properties, that is,  $\beta = \arctan 2(\sin(\beta), \cos(\beta))$  and  $\alpha = \arctan 2(\sin(\alpha), \cos(\alpha))$ . The  $\alpha$  and  $\beta$  angles define the pairwise transformation from frame  $r$  to  $l$  in *global* space, which finalizes *local* registration between two frames.

## 5 Experiment and Evaluation

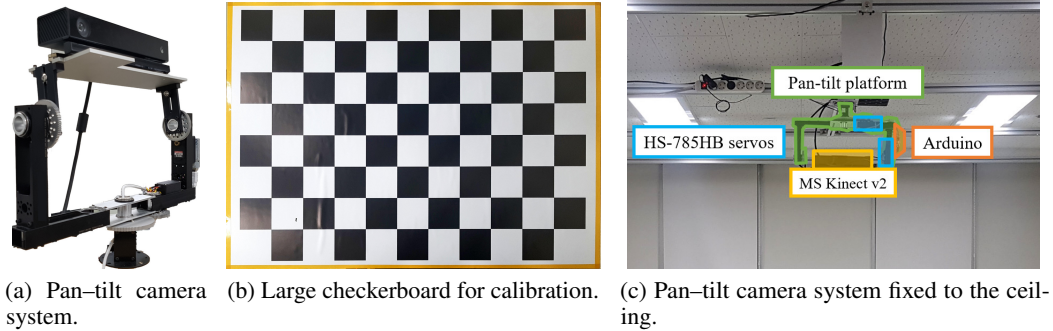


Figure 8: Pan-tilt RGB-D scan registration configuration.

### 5.1 System and Dataset Configuration

To validate the proposed method, an experimental environment was set up comprising an RGB-D camera and two servo motors that rotate in *pan* and *tilt* directions, supported by a steerable platform, with an external large-sized checkerboard for calibration purposes. The checkerboard consists of  $8 \times 11$  black-and-white checkers, which implies that there are seven rows and ten columns of corner points. The size of a checker, or the distance between corners, is 100 mm vertically and horizontally. The steerable platform was assembled from custom-made arms and gears, where two servos were attached to rotate the platform horizontally and vertically. Two HS-785HB servo motors were used, which accept 600–2400 microseconds pulse width. The model is a so-called *hobby servo*, which costs approximately 50.00 USD and can rotate with an acceptable accuracy; however, it is not industry-grade. For the RGB-D camera, Microsoft Kinect v2 was used, supporting up to  $1920 \times 1080$  RGB stream and  $512 \times 424$  time-of-flight depth stream in real time. It was mounted on the upper plate of the steerable platform. The setup used in the pan-tilt scan registration is shown in Figure 8.

The proposed approach, similar to that in [18], combines servo control and camera pose estimation for point cloud registration. Thus, calibration data, including rotation axes and pulse width mapping, is required as well as color images, depth images, and point cloud data. However, to the best of the authors’ knowledge, there is no publicly available dataset that meets all the requirements for pan-tilt RGB-D scan registration, including the dataset in [18]. Therefore, the pan-tilt RGB-D scan dataset was constructed in-house, using the setup shown in Figure 8. The pan-tilt camera system was fixed to the ceiling, and rotated horizontally and vertically to construct the pan-tilt RGB-D scan dataset.

### 5.2 Pan-Tilt RGB-D Scan Registration

The proposed method was compared with four state-of-art methods that used different approaches. The first is the RGB-D camera calibration (RGBD-Calib) method [18], which makes use of external parameters of the camera for pose estimation. Both the proposed method and the RGB-D camera calibration method can be classified as calibration-based approaches, which require calibrations to be performed beforehand. For both methods, the same sequences of color and depth images were used to calibrate the rotation axes and external camera parameters. Two other methods are the FGR method proposed in [20] and the S4PCS method proposed in [19], which were compared with the RGB-D camera calibration method in [18]. Both methods are global registration methods, which can accept two point clouds of any status and globally search for the point correspondences to perform registration. The last method for comparison is the ORB-SLAM2 [2]. ORB-SLAM2 is one of the most cited SLAM methods, which can compute the trajectory of monocular, stereo, and RGB-D cameras, as well as a sparse 3D reconstruction, provided that the stereo and RGB-D data with true scale is given. ORB-SLAM2 is also known to be a real-time SLAM library if CPU multi-threading is

supported by the OpenMP library. However, as all other methods run in a single process/thread, multi-threading option for ORB-SLAM2 was disabled in the experiments for fairness.

The experiment and error metric were designed as were in [18]. The experiment process is as follows:

1. A pair of pan-tilt RGB-D scans is input to each algorithm, including a color image, a depth image, and point cloud data.
2. A rough transformation between two frames is estimated using the algorithm while its processing is measured.
3. Using the rough registration, the RMS error of  $N$  closest points is measured.
4. The ICP algorithm is used to acquire the fine registration, with the rough estimation as the initial guess input, and the processing time is measured.
5. The RMS error of the fine registration is measured.

All algorithms except for the proposed were tested twice, first without ICP refinement and then with ICP refinement. The proposed algorithm was tested three times: (1) Only global registration, "Proposed (Default)", (Section 4.2) without ICP refinement. (2) Global and local registration, "Proposed (Axis Bound)", (Section 4.3) without ICP refinement. (3) Global and local registration with ICP refinement. This is to better demonstrate the performance of Proposed (Default) with RGBD-Calib [18] in terms of global registration. Moreover, it is to demonstrate the improvement made in Proposed (Axis Bound) by local registration, over Proposed (Default), global registration. In total, eleven variations were derived from five algorithms with different options and tested in the experiments.

To quantitatively measure the performance of the registration results, the RMS metric of  $N$  closest points was used [18]. Given  $N$  points in the input point cloud, or frame  $r$ , their closest points are determined in the source point cloud, or frame  $l$ . If the vector storing the vector distances (in millimeters) between  $N$  closest point pairs is denoted by  $d_{min} \in R^N$  and its  $i$ -th element by  $d_{min}(i)$ , the RMSE is defined as

$$RMS = \sqrt{\frac{\sum_{i=1}^N d_{min}^2(i)}{N}}. \quad (26)$$

All experiments were conducted on a desktop computer running Windows 10 with Intel Core i7-6700K CPU @ 4.00 GHz and 16 GB of DDR4 memory. For image processing and camera calibration, the OpenCV library [35] was used. For ICP algorithm and  $N$  closest points RMSE implementation, the PCL library was used [36]. All codes are written in C++ with the same compiler optimization option and no multi-threading.

### 5.3 Experiment, Evaluation, and Analysis

Table 1: Pan-tilt registration datasets with categories

Pan	Tilt	Pan-Tilt
(a) Scene 0 and 10	(d) Scene 39 and 45	(g) Scene 0 and 47
(b) Scene 0 and 20	(e) Scene 39 and 49	(h) Scene 47 and 37
(c) Scene 0 and 30	(f) Scene 39 and 55	

Figure 9 shows eight pan-tilt scan datasets used for the RGB-D registration experiments. Each subfigure of Figure 9 is used for an independent experiment. In each subfigure, the point cloud on the left is input as frame  $l$ , and on the right point cloud as frame  $r$ . The eight test cases can be classified into three categories as in Table 1, i.e., *pan*, *tilt*, and *pan-tilt*, with respect to how the dataset was created.

The *pan* category includes subfigures (a)–(c) of Figure 9. The *pan* category was created by rotating the pan-tilt camera system in *pan* direction with increasing angles at each step, resulting in decreasing overlapping ratio between two scanned RGB-D frames. The *tilt* category includes subfigures (d)–(f) of Figure 9. The *tilt* category was created by rotating the pan-tilt camera system in the *tilt* direction with increasing angles at each step, resulting in decreasing overlapping ratio between two scanned RGB-D frames. Subfigures (g) and (h) of Figure 9 are classified as *pan-tilt*, which entails random rotations in both *pan* and *tilt* directions.

The registration results of input RGB-D scans (a)–(h) of five algorithms are respectively shown as Figures A.1–A.8 in the supplementary material. Tables 2 and 3 show the quantitative results of the comparative registration experiments. It should be emphasized that a fair amount of time was devoted to adjusting parameters for each algorithm, particularly

Table 2: Registration experiment results with ICP refinement. The shortest time to complete is highlighted in yellow. The lowest RMSE is highlighted in red. The algorithm with the lowest RMSE is emboldened. RGBD-Calib [18], ORB-SLAM2 [2], FGR [20], and S4PCS [19] are compared with the proposed method.

(a) Scene 0 and 10			(b) Scene 0 and 20		
Algorithm	Seconds	RMSE	Algorithm	Seconds	RMSE
<b>Proposed (Axis Bound) w/ ICP</b>	<b>6.165796</b>	<b>18.240154</b>	<b>Proposed (Axis Bound) w/ ICP</b>	<b>10.95484</b>	<b>21.018961</b>
RGBD-Calib w/ ICP	7.841424	18.31772	RGBD-Calib w/ ICP	22.772879	21.306742
ORB-SLAM2 w/ ICP	11.518395	18.290323	ORB-SLAM2 w/ ICP	22.969648	21.69693
FGR w/ ICP	97.338219	18.285046	FGR w/ ICP	104.918724	34.579342
S4PCS w/ ICP	507.913788	33.473557	S4PCS w/ ICP	839.813477	24.980606

(c) Scene 0 and 30			(d) Scene 39 and 45		
Algorithm	Seconds	RMSE	Algorithm	Seconds	RMSE
<b>Proposed (Axis Bound) w/ ICP</b>	<b>13.866281</b>	<b>25.031805</b>	Proposed (Axis Bound) w/ ICP	<b>2.691338</b>	18.300602
RGBD-Calib w/ ICP	<b>6.785756</b>	25.219973	<b>RGBD-Calib w/ ICP</b>	<b>6.385001</b>	<b>18.067091</b>
ORB-SLAM2 w/ ICP	17.887688	27.591806	ORB-SLAM2 w/ ICP	5.755304	18.471491
FGR w/ ICP	94.994743	51.435535	FGR w/ ICP	82.637749	18.10957
S4PCS w/ ICP	479.631866	35.960091	S4PCS w/ ICP	858.546326	32.197487

(e) Scene 39 and 49			(f) Scene 39 and 55		
Algorithm	Seconds	RMSE	Algorithm	Seconds	RMSE
Proposed (Axis Bound) w/ ICP	<b>6.49277</b>	20.722336	Proposed (Axis Bound) w/ ICP	<b>10.752523</b>	24.766397
<b>RGBD-Calib w/ ICP</b>	<b>14.649153</b>	<b>19.918831</b>	<b>RGBD-Calib w/ ICP</b>	<b>13.817297</b>	<b>24.273544</b>
ORB-SLAM2 w/ ICP	7.232457	20.215399	ORB-SLAM2 w/ ICP	17.304333	24.329607
FGR w/ ICP	84.597931	20.404255	FGR w/ ICP	96.762566	52.421944
S4PCS w/ ICP	1138.122925	39.033878	S4PCS w/ ICP	689.655518	29.837551

(g) Scene 0 and 47			(h) Scene 47 and 37		
Algorithm	Seconds	RMSE	Algorithm	Seconds	RMSE
<b>Proposed (Axis Bound) w/ ICP</b>	<b>11.312024</b>	<b>22.021082</b>	<b>Proposed (Axis Bound) w/ ICP</b>	<b>24.597227</b>	<b>22.614401</b>
RGBD-Calib w/ ICP	24.272514	22.689531	RGBD-Calib w/ ICP	51.139652	23.089069
ORB-SLAM2 w/ ICP	<b>6.143121</b>	30.789194	ORB-SLAM2 w/ ICP	47.346447	22.760431
FGR w/ ICP	109.689415	52.370953	FGR w/ ICP	103.696716	37.848007
S4PCS w/ ICP	1654.033569	26.767384	S4PCS w/ ICP	409.787476	34.307533

FGR and S4PCS, to optimize the algorithm in terms of RMSE. Moreover, the termination conditions for the ICP algorithm in terms of convergence and exit refinement were optimized and fixed throughout the experiments. In Tables 3 and 2, the algorithms with best results in terms of the lowest RMSE are emboldened, with their results highlighted in red. Numbers highlighted in yellow indicate the time for the fastest algorithm to complete registration.

### 5.3.1 Algorithms with ICP refinement

The performance results of the algorithms with ICP refinement are first examined. In terms of accuracy, the proposed method with ICP, called "Proposed (Axis Bound) w/ ICP", yielded the best RMSE results in five out of eight test experiments. In the experiments (d), (e), and (f), in which the proposed method did not rank first, "RGBD-Calib w/ ICP" yielded the best RMSE results. The datasets (d), (e), and (f) are categorized as "Tilt" in Table 1. The Tilt dataset was created with the camera facing directly at the front wall and tilting by certain amounts. As the checkerboard was placed in parallel to the wall in the camera calibration process in the RGBD-Calib method, it is conjectured that this planar-aligned calibration affected the external parameter calibration quality and, in turn, the registration results qualities. Nevertheless, the proposed method performed quite comparably even in such cases.

In general, it is quite apparent that the global registration methods, FGR and S4PCS, performed in general poorly even with ICP refinement. It becomes clearer if one examines figures in Appendix that the two global registration methods sometimes completely fail to perform reasonable registration. It is conceivable that the two algorithms are originally designed to match 3D scans of an object, thus performing poorly when registering two partial point clouds of a room geometry with low overlapping ratio and a large number of multiple occurring features such as corners and planes.

In terms of speed, in six out of eight experiments, the proposed method with ICP refinement required the least time to meet the termination requirement of the ICP algorithm. In the other two experiments, the proposed method with ICP

Table 3: Registration experiment results without ICP refinement. The shortest time to complete is highlighted in yellow. The lowest RMSE is highlighted in red. The algorithm with the lowest RMSE is emboldened. RGBD-Calib [18], ORB-SLAM2 [2], FGR [20], and S4PCS [19] are compared with the proposed method.

(a) Scene 0 and 10			(b) Scene 0 and 20		
Algorithm	Seconds	RMSE	Algorithm	Seconds	RMSE
Proposed (Default)	0.000246	24.216434	Proposed (Default)	0.000152	39.480484
Proposed (Axis Bound)	0.216397	22.089104	<b>Proposed (Axis Bound)</b>	<b>0.192879</b>	<b>26.342659</b>
RGBD-Calib	0.000253	25.840878	RGBD-Calib	0.0003	44.22562
ORB-SLAM2	1.074861	23.478292	ORB-SLAM2	1.023496	33.239819
<b>FGR</b>	<b>97.661324</b>	<b>18.544088</b>	FGR	88.800407	43.18259
S4PCS	506.601318	34.0005	S4PCS	813.314758	26.734369

(c) Scene 0 and 30			(d) Scene 39 and 45		
Algorithm	Seconds	RMSE	Algorithm	Seconds	RMSE
Proposed (Default)	0.000152	29.798969	Proposed (Default)	0.000153	22.617462
Proposed (Axis Bound)	0.182541	29.480431	Proposed (Axis Bound)	0.200695	18.494429
<b>RGBD-Calib</b>	<b>0.000223</b>	<b>27.886969</b>	RGBD-Calib	0.000229	26.905491
ORB-SLAM2	0.997898	39.125057	ORB-SLAM2	1.073492	22.734163
FGR	89.779678	53.558205	<b>FGR</b>	<b>80.843987</b>	<b>18.279284</b>
S4PCS	470.615967	36.979393	S4PCS	849.497375	36.19183

(e) Scene 39 and 49			(f) Scene 39 and 55		
Algorithm	Seconds	RMSE	Algorithm	Seconds	RMSE
Proposed (Default)	0.00016	35.338062	Proposed (Default)	0.000157	40.294407
Proposed (Axis Bound)	0.187851	21.70833	<b>Proposed (Axis Bound)</b>	<b>0.200255</b>	<b>26.52479</b>
RGBD-Calib	0.000268	26.994507	RGBD-Calib	0.000267	28.377275
ORB-SLAM2	0.989275	21.250082	ORB-SLAM2	0.871645	29.009817
<b>FGR</b>	<b>84.577904</b>	<b>20.597624</b>	FGR	96.257271	52.473236
S4PCS	1124.515869	41.079308	S4PCS	690.405457	32.846741

(g) Scene 0 and 47			(h) Scene 47 and 37		
Algorithm	Seconds	RMSE	Algorithm	Seconds	RMSE
Proposed (Default)	0.000157	39.12294	Proposed (Default)	0.000155	37.162189
<b>Proposed (Axis Bound)</b>	<b>0.193834</b>	<b>28.088261</b>	<b>Proposed (Axis Bound)</b>	<b>0.186479</b>	<b>32.014629</b>
RGBD-Calib	0.000245	38.565479	RGBD-Calib	0.000245	32.599045
ORB-SLAM2	1.060248	33.096642	ORB-SLAM2	0.994338	43.82259
FGR	99.504509	51.898098	FGR	93.62558	39.974655
S4PCS	1670.844849	31.175213	S4PCS	220.25766	40.932125

refinement was the second fastest algorithm. It is noticeable that in several cases, the proposed method was twice as fast as the second and exhibited comparable or better performance results, as in experiments (b), (d), and (e). In general, feature matching-based algorithms, including the proposed method and ORB-SLAM2 method, were faster.

Furthermore, FGR performed better than or comparably to S4PCS and maintained quite constant computation time, i.e., approximately 100 seconds, whereas S4PCS exhibited radically varying timings of 500, 800, and 1000–1600 seconds.

### 5.3.2 Algorithms without ICP refinement

The algorithms without ICP refinement are now considered. The speed comparison between the two calibration-based approaches, "Proposed (Default)" and RGBD-Calib, is as follows. As explained above, Proposed (Default) derives the transformation estimation only from the servo control and its rotation transformation, i.e., Equations 13 and 8. By contrast, RGBD-Calib uses external parameters of the camera calibration to estimate camera poses. Even though the two algorithms have comparable RMSE performance, Proposed (Default) is always faster than RGBD-Calib. This is because the camera pose look-up table of RGBD-Calib requires  $O(n)$  time (it was implemented with `std::map::find` of C++ STL), whereas Equations 13 and 8 of the proposed method require  $O(1)$  time regardless of the number of pan-tilt camera poses used in the calibration.

The two feature-matching-based algorithms, Proposed (Axis Bound) and ORB-SLAM2, are also worth examining. Proposed (Axis Bound) has lower RMSE in seven experiments, except only for "(e) Scene 39 and 40". Moreover, Proposed (Axis Bound) completed in approximately 0.2 seconds, whereas ORB-SLAM2 in approximately 1 second. It is conceivable that the proposed *axis bound registration* method (Section 4.3.2) captures the geometric and kinetic characteristics of the pan-tilt rotations and exploits them in RGB-D scan registration, resulting in fast and accurate registration.

In conclusion, the proposed method achieved optimal results with and without ICP refinement. This implies that the proposed method can provide a valid starting point, or the "right track", that leads the ICP algorithm to better results, preventing the algorithm from being stuck in a local optimum. In addition to providing accurate results, the proposed method was faster even with the ICP refinement process. This indicates that the proposed algorithm can produce an initial registration result that is very close to the optimal solution. Consequently, the proposed method performed at least comparably to, and often outperformed, other state-of-the-art registration algorithms in terms of computational accuracy (RMSE), speed, and thus efficiency.

## 6 Conclusion

*Axis bound registration* was proposed, which is a novel method for registering RGB-D scans of a pan-tilt camera. Through the rotation axis calibration and camera-servo control, the proposed method recovers the rotation parameters and its transformation model. The prior knowledge on the rotational motion of the pan-tilt servos leads to a novel distance-to-rotation-trajectory constraint that is used to reject false matching of keypoints between two frames without an iterative and time-consuming random sample consensus (RANSAC) process. The recovered transformation model is used to construct an objective function that minimizes the error in point-to-point matching. The (empirically one-step) alternating optimization scheme is adopted to divide the objective function into two independent problems, i.e., determining *pan* and *tilt* rotations, that can be solved in a closed form, and it ultimately accelerates optimization convergence. In the experiments, the proposed method was compared with four other state-of-the-art registration algorithms and tested for the RMSE of distances to  $N$  closest points and computation time. In five out of seven experiment conditions, the proposed method outperformed the other registration methods by great margins in terms of both RMSE and speed. This demonstrates that the proposed method can provide more accurate and efficient solutions for point cloud registration.

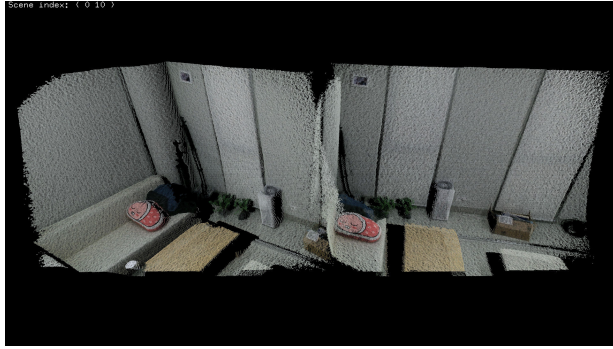
In the future, the proposed algorithm should be extended to incorporate online, dense, and volumetric reconstruction that continuously updates constructed 3D scenes with dynamic objects.

## References

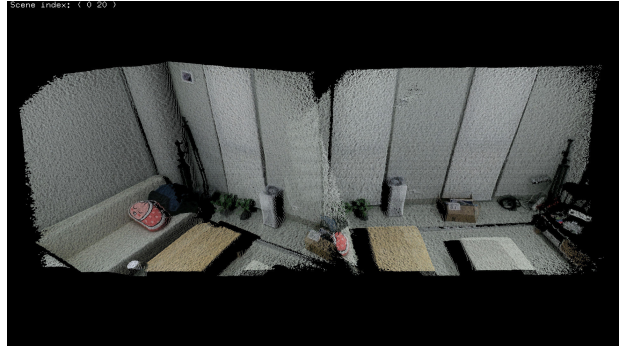
- [1] Peter Henry, Michael Krainin, Evan Herbst, Xiaofeng Ren, and Dieter Fox. Rgb-d mapping: Using depth cameras for dense 3d modeling of indoor environments. In *In the 12th International Symposium on Experimental Robotics (ISER)*. Citeseer, 2010.
- [2] Raúl Mur-Artal and Juan D. Tardós. ORB-SLAM2: an open-source SLAM system for monocular, stereo and RGB-D cameras. *IEEE Transactions on Robotics*, 33(5):1255–1262, 2017.
- [3] Satoshi Ikehata, Hang Yang, and Yasutaka Furukawa. Structured indoor modeling. In *Proceedings of the IEEE International Conference on Computer Vision*, pages 1323–1331, 2015.
- [4] Daniel Kurz, Ferry Hantsch, Max Grobe, Alexander Schiewe, and Oliver Bimber. Laser pointer tracking in projector-augmented architectural environments. In *Mixed and Augmented Reality, 2007. ISMAR 2007. 6th IEEE and ACM International Symposium on*, pages 19–26. IEEE, 2007.
- [5] Andrew Wilson, Hrvoje Benko, Shahram Izadi, and Otmar Hilliges. Steerable augmented reality with the beamatron. In *Proceedings of the 25th annual ACM symposium on User interface software and technology*, pages 413–422. ACM, 2012.
- [6] Jung-Hyun Byun, Seung-Ho Chae, Yoon-Sik Yang, and Tack-Don Han. AIR: Anywhere Immersive Reality with User-Perspective Projection. In *EG 2017 - Short Papers*. The Eurographics Association, 2017.
- [7] J. Sturm, N. Engelhard, F. Endres, W. Burgard, and D. Cremers. A benchmark for the evaluation of rgb-d slam systems. In *Proc. of the International Conference on Intelligent Robot Systems (IROS)*, Oct. 2012.
- [8] Asad Ullah Naweed, Lu Chen, Mingsong Dou, and Henry Fuchs. Enhancement of 3d capture of room-sized dynamic scenes with pan-tilt-zoom cameras. In *International Symposium on Visual Computing*, pages 379–389. Springer, 2014.

- [9] Rareş Ambruş, Nils Bore, John Folkesson, and Patric Jensfelt. Meta-rooms: Building and maintaining long term spatial models in a dynamic world. In *Intelligent Robots and Systems (IROS 2014), 2014 IEEE/RSJ International Conference on*, pages 1854–1861. IEEE, 2014.
- [10] Zhenqi Niu, Kuo Liu, Yuemin Wang, Shujun Huang, Xiaoting Deng, and Zonghua Zhang. Calibration method for the relative orientation between the rotation axis and a camera using constrained global optimization. *Measurement Science and Technology*, 28(5):055001, 2017.
- [11] Richard A Newcombe, Shahram Izadi, Otmar Hilliges, David Molyneaux, David Kim, Andrew J Davison, Pushmeet Kohi, Jamie Shotton, Steve Hodges, and Andrew Fitzgibbon. Kinectfusion: Real-time dense surface mapping and tracking. In *Mixed and augmented reality (ISMAR), 2011 10th IEEE international symposium on*, pages 127–136. IEEE, 2011.
- [12] Paul J Besl, Neil D McKay, et al. A method for registration of 3-d shapes. *IEEE Transactions on pattern analysis and machine intelligence*, 14(2):239–256, 1992.
- [13] Dominik Neumann, Felix Lugauer, Sebastian Bauer, Jakob Wasza, and Joachim Hornegger. Real-time rgb-d mapping and 3-d modeling on the gpu using the random ball cover data structure. In *Computer Vision Workshops (ICCV Workshops), 2011 IEEE International Conference on*, pages 1161–1167. IEEE, 2011.
- [14] James Davis and Xing Chen. Calibrating pan-tilt cameras in wide-area surveillance networks. In *In IEEE International Conference on Computer Vision*. Citeseer, 2003.
- [15] Ziyang Wu and Richard J Radke. Keeping a pan-tilt-zoom camera calibrated. *IEEE transactions on pattern analysis and machine intelligence*, 35(8):1994–2007, 2013.
- [16] Ping Chen, Min Dai, Kai Chen, and Zhisheng Zhang. Rotation axis calibration of a turntable using constrained global optimization. *Optik-International Journal for Light and Electron Optics*, 125(17):4831–4836, 2014.
- [17] Jung-Hyun Byun, Seung-Ho Chae, and Tack-Don Han. Accurate Control of a Pan-tilt System Based on Parameterization of Rotational Motion. In *EG 2018 - Short Papers*. The Eurographics Association, 2018.
- [18] Chi-Yi Tsai and Chih-Hung Huang. Indoor scene point cloud registration algorithm based on rgb-d camera calibration. *Sensors*, 17(8):1874, 2017.
- [19] Nicolas Mellado, Dror Aiger, and Niloy J Mitra. Super 4pcs fast global pointcloud registration via smart indexing. In *Computer Graphics Forum*, volume 33, pages 205–215. Wiley Online Library, 2014.
- [20] Qian-Yi Zhou, Jaesik Park, and Vladlen Koltun. Fast global registration. In *European Conference on Computer Vision*, pages 766–782. Springer, 2016.
- [21] Dror Aiger, Niloy J Mitra, and Daniel Cohen-Or. 4-points congruent sets for robust pairwise surface registration. In *ACM Transactions on Graphics (TOG)*, volume 27, page 85. ACM, 2008.
- [22] Andrew J Davison. Real-time simultaneous localisation and mapping with a single camera. In *Computer Vision (ICCV), 2003 IEEE International Conference on*, page 1403. IEEE, 2003.
- [23] Georg Klein and David Murray. Parallel tracking and mapping for small ar workspaces. In *Mixed and Augmented Reality, 2007. ISMAR 2007. 6th IEEE and ACM International Symposium on*, pages 225–234. IEEE, 2007.
- [24] Richard A Newcombe, Steven J Lovegrove, and Andrew J Davison. Dtam: Dense tracking and mapping in real-time. In *Computer Vision (ICCV), 2011 IEEE International Conference on*, pages 2320–2327. IEEE, 2011.
- [25] Felix Endres, Jürgen Hess, Jürgen Sturm, Daniel Cremers, and Wolfram Burgard. 3-d mapping with an rgb-d camera. *IEEE Transactions on Robotics*, 30(1):177–187, 2014.
- [26] Ellon Mendes, Pierrick Koch, and Simon Lacroix. Icp-based pose-graph slam. In *Safety, Security, and Rescue Robotics (SSRR), 2016 IEEE International Symposium on*, pages 195–200. IEEE, 2016.
- [27] T. Whelan, R. F. Salas-Moreno, B. Glocker, A. J. Davison, and S. Leutenegger. Elasticfusion: Real-time dense slam and light source estimation. *Intl. J. of Robotics Research, IJRR*, 2016.
- [28] Burkhard Schaffrin. A note on constrained total least-squares estimation. *Linear algebra and its applications*, 417(1):245–258, 2006.
- [29] Ethan Rublee, Vincent Rabaud, Kurt Konolige, and Gary Bradski. Orb: An efficient alternative to sift or surf. In *Computer Vision (ICCV), 2011 IEEE international conference on*, pages 2564–2571. IEEE, 2011.
- [30] Seungho Chae, Yoonsik Yang, Heeseung Choi, Ig-Jae Kim, Junghyun Byun, Jiyeon Jo, and Tack-Don Han. Smart advisor: Real-time information provider with mobile augmented reality. In *Consumer Electronics (ICCE), 2016 IEEE International Conference on*, pages 97–98. IEEE, 2016.

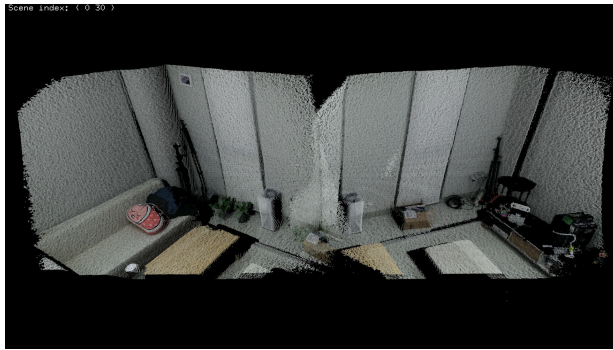
- [31] Ben Bellekens, Vincent Spruyt, Rafael Berkvens, and Maarten Weyn. A survey of rigid 3d pointcloud registration algorithms. In *AMBIENT 2014: the Fourth International Conference on Ambient Computing, Applications, Services and Technologies, August 24-28, 2014, Rome, Italy*, pages 8–13, 2014.
- [32] Samuel R Buss. Introduction to inverse kinematics with jacobian transpose, pseudoinverse and damped least squares methods. *IEEE Journal of Robotics and Automation*, 17(1-19):16, 2004.
- [33] Adrian Kaehler and Gary Bradski. *Learning OpenCV 3: computer vision in C++ with the OpenCV library*. " O'Reilly Media, Inc.", 2016.
- [34] Qian-Yi Zhou and Vladlen Koltun. Color map optimization for 3d reconstruction with consumer depth cameras. *ACM Transactions on Graphics (TOG)*, 33(4):155, 2014.
- [35] G. Bradski. The OpenCV Library. *Dr. Dobb's Journal of Software Tools*, 2000.
- [36] Radu Bogdan Rusu and Steve Cousins. 3D is here: Point Cloud Library (PCL). In *IEEE International Conference on Robotics and Automation (ICRA)*, Shanghai, China, May 9-13 2011.



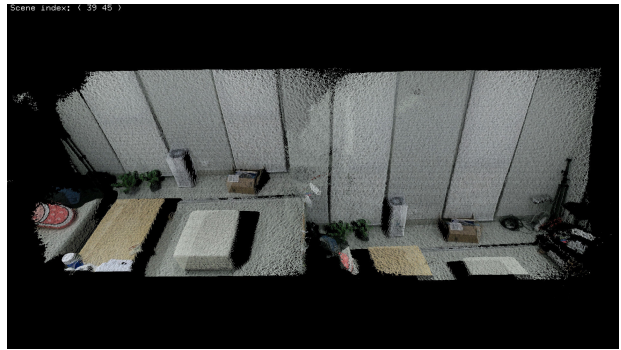
(a) Scene 0 and 10



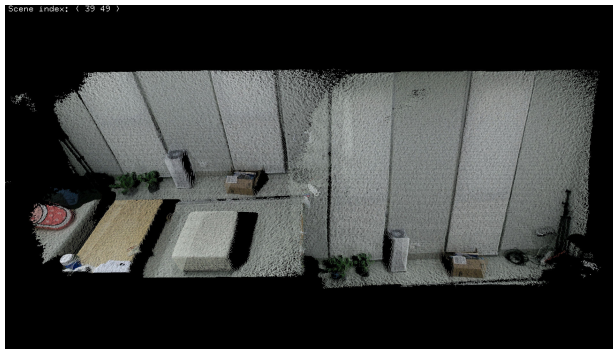
(b) Scene 0 and 20



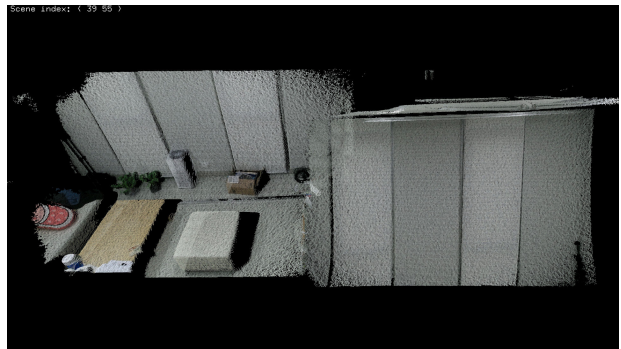
(c) Scene 0 and 30



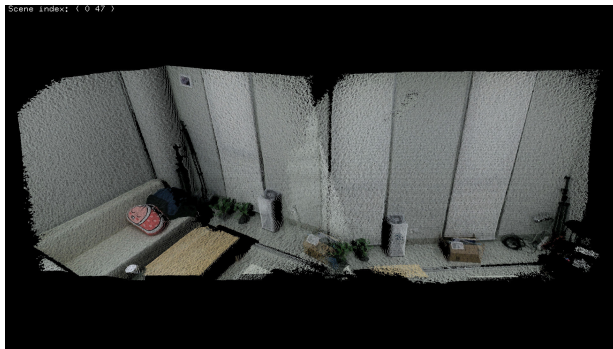
(d) Scene 39 and 45



(e) Scene 39 and 49



(f) Scene 39 and 55



(g) Scene 0 and 47



(h) Scene 47 and 37

Figure 9: Datasets used for pan-tilt RGB-D scan registration. Point clouds on the left in each image are frame  $l$ , or the target point clouds. Point clouds on the right in each image are frame  $r$ , or the source point clouds. The shown layout of point clouds is for visualization purpose only.